sustainability

MDPI

Article

Removal and Recovery of Europium with a New Functionalized Mesoporous Silica-Based Adsorbent

Charith Fonseka [1], Seongchul Ryu [1], Jaya Kandasamy [1,*], Harsha Ratnaweera [2] and Saravanamuthu Vigneswaran [1,2,*]

[1] Faculty of Engineering, University of Technology Sydney (UTS), P.O. Box 123, Broadway, NSW 2127, Australia; charithjude@gmail.com (C.F.); seongchul91@gmail.com (S.R.)
[2] Faculty of Sciences and Technology (RealTek), Norwegian University of Life Sciences, P.O. Box 5003, NO-1432 Ås, Norway; harsha.ratnaweera@nmbu.no
* Correspondence: jaya.kandasamy@uts.edu.au (J.K.); saravanamuth.vigneswaran@uts.edu.au (S.V.)

Abstract: The discharge of acid mine drainage (AMD), characterized by a high concentration of rare earth elements (REEs), poses a significant threat to the health of ecosystems surrounding water sources. The global market demand for REEs has experienced a notable surge in the past decade. Consequently, recovering REEs from waste streams like AMD not only benefits the environment but also offers financial advantages. Europium (Eu), the rarest among REEs, constitutes only 0.1% w/w in monazite and bastnaesite ores. Eu is extensively used in the production of phosphors, alloys, and additives, and is a critical raw material for developing smart devices, ranging from high-resolution color screens to circuitry. Traditional adsorbents typically exhibit limited selectivity towards REE recovery. Mesoporous silica materials, such as SBA15 (Santa Barbara Amorphous-15), provide excellent tunability and modification capabilities, making them an attractive and cost-effective alternative. This research focused on two key aspects: (i) evaluating the dynamic adsorption column performance of granulated SBA15–NH–PMIDA to preferentially recover Eu, and (ii) employing mathematical modeling to optimize the dynamic adsorption column's operating conditions for real-world applications with a minimal number of experimental runs. Granulated SBA15–NH–PMIDA was chosen as the adsorbent due to its high adsorptive capacity and selectivity in capturing Eu. The study revealed that granulated SBA15–NH–PMIDA exhibited 57.47 mg/g adsorption capacity and an 81% selectivity towards Eu. Furthermore, SBA15–NH–PMIDA demonstrated preferential adsorption toward Eu in complex multi-component solutions, such as AMD. The linear driven force approximation model (LDFAM) provided an acceptable simulation ($R^2 > 0.91$) under varying operational conditions. This validates the use of the model as a tool to effectively simulate and optimize column experiments that used granulated SBA15–NH–PMIDA to recover Eu.

Keywords: acid mine drainage; rare earth elements; adsorbents; modeling

Citation: Fonseka, C.; Ryu, S.; Kandasamy, J.; Ratnaweera, H.; Vigneswaran, S. Removal and Recovery of Europium with a New Functionalized Mesoporous Silica-Based Adsorbent. *Sustainability* **2024**, *16*, 5636. https://doi.org/10.3390/su16135636

Academic Editor: Luca Di Palma

Received: 1 June 2024
Revised: 25 June 2024
Accepted: 27 June 2024
Published: 30 June 2024

1. Introduction

Acid mine drainage (AMD), resulting from water seepage through ore waste piles, exposed earth cuts, and sulfur-rich soil, poses a significant environmental concern for countries with abandoned or active mining sites [1]. AMD pollution has the potential to severely impact the health of ecosystems surrounding water sources, leading to the accumulation of heavy metals and rare earth elements (REE) in the food chain, thereby posing health risks to humans. Therefore, identifying efficient and cost-effective methods for treating AMD is crucial [1].

The group of rare earth elements (REEs) comprises 17 chemical elements in the periodic table, including 15 lanthanides, yttrium, and scandium [2]. The concentration of REEs in AMD waters is found to be higher than that in surface water bodies [3,4]. The chemical composition of mining wastewater in Northern Norway is given in Table 1 [5]. Pyrite

oxidation is the primary reaction responsible for generating AMD. The resulting high acidity leads to the leaching of adjacent rocks, causing additional metals to dissolve in water [6]. Among the metals commonly found in AMD waters, iron (Fe) and aluminum (Al) are the most prevalent [7,8]. While the behavior of heavy metals in AMD has been extensively studied, there is limited data on the concentrations of rare earth elements in AMD. This scarcity of data can be attributed to the relatively lower toxicity of REEs compared to heavy metals. However, recent studies have demonstrated that elevated concentrations of REEs in water can pose significant health concerns for both humans and animals [9]. Table 2 presents the selective presence of REEs in AMD from various countries. With increased global mining activities, the probability of surface and groundwater contamination with REEs is on the rise, leading to the accumulation of REEs in plants and animals and potential severe environmental and health impacts.

Table 1. Composition of AMD obtained from abandoned mining site in Norway (pH = 2.1 ± 0.1) (modified from Fonseka et al. [5]).

Dissolved Ions	Na	Mg	Al	S	Ca	Cr	Mn	Fe	Ni	Cu	Zn	Eu
Concentration (mg/L)	36	218	168	1275	187	0.38	6.29	618	0.51	62	39	3.1

Table 2. The chemical composition of AMD in different countries (mg/L) (modified from Fonseka [5]).

Location	pH	La	Ce	Pr	Nd	Sm	Eu	Gd	Tb	Dy	Ho	Er	Tm	Yb	Lu	Total REE	Reference
Jaintia Hills INDIA	3.0	91.8	284.9	38.4	121.0	38.4	9.1	44.2	7.3	34.4	8.8	15.7	3.6	13.2	3.4	714.7	[10]
Sitai Coal Mine CHINA	3.6	7.7	19.3	2.7	12.9	2.9	0.8	3.7	0.7	4.0	0.8	2.4	0.3	1.9	0.3	61.2	[6]
Osamu Utsumi Mine BRAZIL	4.4	567.0	124.0	0.0	250.0	28.5	7.7	22.6	0.0	23.2	5.2	12.2	0.0	5.5	0.5	1046.7	[11]
Metalliferous Hills ITALY	3.1	185.0	389.5	45.7	172.2	34.8	8.6	40.1	5.0	23.6	4.1	10.5	1.2	7.0	0.9	928.83	[12]
West Virginia USA	4.2	11.4	41.5	7.0	39.1	13.9	3.9	19.2	3.0	16.5	2.9	7.7	1.2	5.5	1.0	174.39	[13]
Huelva Estuary	1.6	1780	4480	590.0	2580	614.0	65.4	554.0	54.7	253.0	37.2	85.9	10.2	61.7	7.6	11173	[14]
Odiel Rive Spain	4.5	331.2	977.2	120.2	545.4	137.3	25.4	152.9	21.1	110.3	19.5	48.0	5.8	33.7	4.6	2532.9	[15]
Lake Tyrell, Victoria Australia	3.7	90.0	279.2	39.5	153.0	31.9	7.9	50.2	5.4	40.5	4.6	13.7	1.8	6.9	0.7	725.7	[16]

The demand for rare earth elements in the global market has risen over the past decade [17]. According to Naidu et al. [1] and Anastopoulos et al. [18], over 90% of the global REE demand is met by China. Recent trade restrictions imposed by China on REE exports have resulted in a severe shortage in the global market [18]. Recognizing the economic importance and low availability of REEs, the European Commission included REEs in the list of critical raw materials in 2014 and 2017 [19,20]. The United States of America also listed REEs among its 35 critical minerals in 2018 [21]. REEs play a vital role in the manufacturing processes of optical fibers, super magnets, superconductors, aerospace alloys, etc. [22]. Therefore, the recovery of REEs from waste, such as AMD, not only benefits the environment but also offers financial advantages.

The increasing demand for high-tech products, cleaner energy technologies, and defense applications has elevated the importance of REEs in the worldwide market. As researchers worldwide work towards ensuring consistent and sustainable access to these essential elements, there is ongoing interest and investment in research and development related to mining, processing, recycling, and diversifying the sources of supply. In the context of AMD, REEs are often present in low concentrations but are of significant interest

due to their potential enrichment and recycling opportunities. Among REEs, europium (Eu) is considered the rarest, constituting only 0.1% *w*/*w* in monazite and bastnaesite ores [23]. Financial constraints have resulted in europium being mined only as a byproduct. Europium is widely used in the production of phosphors, alloys, and additives, and is a critical raw material for the development of smart devices, including high-resolution color screens and circuitry. Europium oxide, as a neutron absorber, has important applications in the nuclear industry, for fast breeder reactors.

Chemical precipitation, ion exchange, solvent extraction, and adsorption are among the more promising methods proposed for REE recovery [4,18,24–26]. According to Kumari et al. [23], membrane distillation and reverse osmosis methods are applied to preconcentrate AMD prior to the selective recovery of REEs [5,27]. Among these methods, adsorption has been found to be the most effective. Nano carbon shells, nano magnetic particles, modified silica composites, and biosorbents have shown efficiency in removing REEs from aqueous media [28–32]. Although these materials exhibit high removal efficiency, increased costs and low regeneration capacity pose barriers to implementing these technologies in practice [33]. Therefore, there is a need for the development of adsorbents that are low-cost, easily sourced, and possess a high adsorption and regeneration capacity for the selective recovery of REEs from AMD. This will enable widespread use of the technology and facilitate the creation of a circular economy for rare earth elements in the international market.

Technologies for industrial wastewater remediation are evolving rapidly to meet the rising demand for clean water. Metal–organic frameworks (MOFs), a group of new-age materials, are extensively explored for resource recovery from wastewater due to their high stability and accessible functionalities. Most traditional adsorbents exhibit limited selectivity towards REE recovery [34]. These adsorbents can be modified with functional groups that can improve its performance. Metal–organic framework (MOF) adsorbents functionalized with specific ligands have shown a high affinity towards REEs [34–36]. However, the high cost of production, coupled with concerns over long-term stability, at this stage prevents the application of these materials on an industrial scale. Mesoporous silica materials, such as SBA15, offer excellent tunability and modification capabilities, making them an attractive, low-cost alternative [37]. As shown in Table S2, novel SBA15–NH–PMIDA material demonstrated a notable affinity for Eu even in the presence of competing tri-valent metals such as iron (Fe) and aluminum (Al) [5]. This suggests that the material could be highly selective for Eu, potentially enabling efficient separation and recovery processes for this rare earth element from complex mixtures like AMD. Hence, there is considerable potential for granulating this material and improving the effectiveness of the adsorption process. This research aimed to study (i) the dynamic adsorption column performance of granulated SBA15–NH–PMIDA to preferentially recover Eu and (ii) mathematical modeling to optimize the dynamic adsorption column operating conditions for real-world applications with a minimum number of experimental runs. Granulated SBA15–NH–PMIDA was chosen as the adsorbent due to its high adsorptive capacity and selective recovery in adsorbing Eu.

2. Materials and Methods

2.1. SBA15–NH–PMIDA Synthesis Process

Tetraethyl orthosilicate (TEOS) (98%, Sigma-Aldrich, St. Louis, MO, USA), poly(ethylene glycol)-block-poly(propylene glycol)-block-poly(ethylene glycol) (P123), (3-aminopropyl) triethoxysilane (APTES, Sigma-Aldrich), *N*,*N*-dicyclohexylcarbodiimide (DCC, 99%), *N*-(phosphonomethyl) iminodiacetic acid (PMIDA, 95%), *N*,*N*-dimethylformamide (DMF, 99%), 34% hydrochloric acid (HCl) solution, toluene (anhydrous, 99.8%), and methyl alcohol (CH_3OH, 99.8%) were used to synthesize SBA15–NH–PMIDA. All chemicals were obtained from Sigma-Aldrich. Sodium alginate (alginic acid sodium salt, medium viscosity, Sigma-Aldrich) and calcium chloride (anhydrous granular, ≥93%) were used to granulate SBA15–NH–PMIDA powder.

SBA-15 was prepared via a hydrothermal reaction [38,39]. A total of 120 mL of 2 M hydrochloric acid (HCl), 23 mL of deionized water (DI-water), and 3.0 g of P123, acting as structure-directing agents, were dissolved at room temperature (24 °C). A total of 6.5 g of TEOS was then added to this solution as a silica source. The mixture was placed in a 200 mL stainless steel hydrothermal synthesis autoclave reactor with PTFE Liner and subjected to aging (self-assembly reaction) at 35 °C for 20 h and 100 °C for an additional 24 h. This step promotes the formation of the mesoporous structure. The residual material was filtered and oven dried at 80 °C overnight. Finally, the powder was calcined at 550 °C for 3 h to remove any remaining water molecules and P123 surfactant [40,41].

2.1.1. Amine Grafting on SBA15

In this step, amine groups were introduced onto the surface of SBA15 for the purpose of enhancing the adsorption and functional properties, based on a previously reported method [39,42]. In total, 1.0 g of SBA15 was mixed into 100 mL of dry toluene. APTES (1 mL) was then added into the solution. The mixture was refluxed at 110 °C for 10 h to allow the reaction between the amino–propyl groups of APTES and the OH groups on the surface of the mesoporous silica. The SBA15–NH_2 precipitate was finally filtered, washed with ethanol, and oven dried at 70 °C.

2.1.2. Synthesis of SBA15–NH–PMIDA

In this study, SBA15–NH_2 was modified with PMIDA. PMIDA grafting of chromium-based MOF was used as a reference [5]. According to Lee et al. [43], a 1:1.5:2 molar ratio between NH_2, PMIDA, and *N*,*N*-dicyclohexylcarbodiimide (DCC) was found as optimal for successful reaction. In SBA-NH_2, 3 moles of SiO_2 bind with 2 moles of NH_2. Therefore, a 1.5 (SBA15–NH_2):1.5 (PMIDA):2 (DCC) molar ratio was calculated to be optimal for synthesis. SBA15–NH_2, PMIDA, and DCC were mixed at a 1.5:1.5:2 molar ratio and transferred to a round-bottom flask containing 80 mL of *N*,*N*-dimethylformamide (DMF, 99%). The solution was refluxed at 150 °C for over 48 h. DCC was used to catalyze the reaction between the amine groups and PMIDA. The solution was then cooled to room temperature and filtered to obtain white SBA15–NH–PMIDA precipitate. It was washed once with toluene followed by ethanol to remove unreacted ligands from the adsorbent. Lastly, the adsorbent was oven dried at 100 °C for over 12 h.

2.2. Granular SBA15–NH–PMIDA

SBA15–NH–PMIDA in granular form is required for use in column adsorption experiments. To achieve this, SBA15–NH–PMIDA underwent a granulation process employing sodium alginate and $CaCl_2$ solutions [44]. Initially, one gram of SBA15–NH–PMIDA in powder form was stirred with 10 mL of a sodium alginate solution (1.5%). A 50 mL syringe was filled with the mixture. The mixture was slowly released into a 0.05 M $CaCl_2$ solution which was continuously stirred at 100 rpm. The granular media that formed was sieved and then oven-dried for over 12 h at 70 °C. The media had a diameter of 2.0 ± 0.1 mm. Additional details regarding the preparation and characterization of SBA15–NH–PMIDA can be found in [5]. The synthesis was duplicated, and the material was synthesized in multiple batches. The performance of granular SBA15–NH–PMIDA across these different batches were tested to evaluate variation.

2.3. Characterization of Granules

The crystalline structure of powder and granular SBA15–NH–PMIDA was explored using X-ray diffraction (XRD) analysis. A Bruker D8 Discover diffractometer was operated at 40 kV with CuKα1Kα radiation for this analysis and was operated in the range of 0 °C to 55 °C maintaining a 2°/min scan rate.

The isotherm data obtained within $0 < P/P0 < 0.5$ range were used for the calculation of the Brunauer–Emmett–Teller (BET) surface area of the granules. The pore distribution and volume were assessed using the Barrett–Joyner–Halenda (BJH) method. Scanning

electron microscopy (SEM) images were acquired using a Zeiss Supra 55VP (Oberkochen, Germany) instrument.

2.4. Equilibrium Adsorption Studies

Equilibrium experiments for europium (Eu) adsorption on granular SBA15-adsorbent media (SBA15–NH–PMIDA of 0.012 g) were conducted in beakers that contained 50 mL of Eu solution at a suitable pH which was determined from our previous study [5]. Granular SBA15–NH–PMIDA displayed a high preference towards the adsorption of Eu (>81%) from AMD (Table S2). A flat shaker kept the solution contained in the beakers continuously stirred (100 rpm) for 24 h at room temperature of 24 °C. The Eu concentration at the initial and equilibrium stage was determined using an inductively coupled plasma mass spectrometry (ICP-MS, Agilent 7900, Santa Clara, CA, USA).

Single solute europium (Eu). The equations used for the modeling of equilibrium isotherms are given in Equations (1) and (2).

$$\text{Adsorption Capacity: } Q_e = \frac{(C_i - C_e)\,V}{m} \tag{1}$$

$$\text{Langmuir Isotherm: } Q_e = \frac{Q_m b C_e}{1 + b C_e} \tag{2}$$

where C_i: Eu initial concentration (mg/L); V: solution volume (l); C_e: Ei equilibrium concentration (mg/L); Q_e: equilibrium adsorption capacity (mg/g); m: adsorbent mass (g); b: Langmuir Constant (L/mg); Q_m: maximum adsorption capacity (mg/g).

2.5. Kinetic Study

The adsorption rate was determined with kinetic experiments. It also helped assess the mass transfer mechanisms. SBA15–NH–PMIDA granules of 0.012 g were mixed with 50 mL synthetic Eu solutions (single solute) at concentrations of 10 and 20 mg/L at the optimum pH. A flat shaker was used to continuously stir the Eu solution in the beakers for 24 h at a temperature of 24 °C. Within the 24 h, samples were periodically taken, and the Eu concentration was measured with the ICP-MS. At the end of the 24 h period the Eu concentration of the solution that remained in the beaker was measured.

The kinetic modeling employed the surface diffusion model (SDM). SDM was found to better predict adsorption kinetics more realistically [44–51]. In this study, the PDEPE function in MATLAB R2024a was employed to solve the SDM Equations (3)–(5). Further details are provided in [44].

$$\frac{\partial q}{\partial t} = \frac{1}{r^2}\frac{\partial}{\partial r}\left(r^2 D_s \frac{\partial q}{\partial r}\right) \tag{3}$$

Boundary conditions:

$$K_f(C - C_s) = D_s \rho_p \frac{\partial q}{\partial r}\ at\ r = R_p \tag{4}$$

$$\frac{\partial q}{\partial r} = 0\ at\ r = 0 \tag{5}$$

where D_s: effective surface diffusion coefficient (m^2/s); r: radial distance of a spherical particle (m); C_s: concentration of Eu at adsorbent surface (mg/L).

2.6. Column Experiment

Adsorption of Eu onto granular SBA15–NH–PMIDA was assessed with fixed bed column experiments. The granular adsorbent was packed into the column to the predetermined depths (10 and 12.5 cm). The experiment was carried out at 24 ± 1 °C. A gear pump regulated the flow rate of the influent Eu solution. Initially, the column was flushed with milli-Q water to saturate the granular adsorbent. The temporal evolution of the residual Eu

concentration was tracked by collecting samples at various times and analyzed with the ICP-MS (Agilent 7900, USA).

2.7. Column Model

In this study, the linear driving force approximation model (LDFAM) was utilized to characterize adsorption in a continuous flow fixed bed column [52] highlights the widespread application of the LDFAM, owing to its simplicity and consistency. The two-dimensional mass balance is delineated with the plug flow model (Equation (6) in Table 3). To ascertain the fixed bed's external film mass transfer coefficient (k_f), (Equation (7)) (Table 3) is employed [53]. Furthermore, the Wilke–Chang equation (Equation (8)) (Table 3) is employed to determine the molecular diffusivity (D_m), drawing from prior findings [44].

Table 3. Equations used in LDFAM.

References	Equation	Equation. #	Parameters	Boundary Conditions
García-Mateos et al. [54]	$-D_L\frac{\partial^2 C}{\partial z^2}+\frac{\partial(vC)}{\partial z}+\frac{\partial C}{\partial t}+\left(\frac{1-\varepsilon}{\varepsilon}\right)\frac{\partial q}{\partial t}=0$	(6)	C = Eu concentration v = superficial velocity D_L = axial dispersion coefficient L = length of column ε = bed porosity	$C = C_0$ at $z = 0$ and $t = 0$ $C = 0$ when $0 < z < L$ and $t = 0$ $D_L\frac{\partial C}{\partial z} = -v(C_0 - C)$ when $z = 0$ and $t > 0$ $\frac{\partial C}{\partial Z} = 0$ when $z = L$ and $t = 0$ Lin et al. [55]
Wakao and Funazkri [56]	$k_f = \frac{D_m}{2R_p}\left(2 + 1.1Re^{0.6}Sc^{0.33}\right)$ $Re = \frac{2R_p v_s \rho_f}{\mu}$ $Sc = \frac{\mu}{D_m \rho_f}$	(7)	Re = Reynold's number Sc = Schmidt number v_s = superficial velocity μ = viscosity of fluid (0.00089 $kgm^{-1}\ s^{-1}$) ρ_f = density of fluid (1000 kg/m^3).	
Wilke and Chang [53], Gomaa et al. [57]	$D_m = 7.4\times10^{-8}\frac{\sqrt{\varnothing M_b}\times T}{\mu V_a^{0.6}}$ $V_a = \frac{M}{\rho} - \frac{(\rho-\rho_0)}{m\rho\rho_0}$	(8)	M_b = molecular weight of Eu $\varnothing$ = association factor T = temperature (K) V_a = molecular volume at boiling temperature M = molarity of solute (mol/kg) m = relative molar mass (kg/mol) ρ = density of solution (g/mL) ρ_0 = density of solvent (g/mL).	

3. Results and Discussion

3.1. Characterization of Granules

The XRD patterns of SBA15, SBA15–NH_2, and pristine SBA15–NH–PMIDA were analyzed. The XRD pattern (refer to Figure S1) of SBA15–NH_2 shows two clear peaks at (1 0 0) and (2 0 0), which corresponds to the hexagonal structure of mesoporous silica [5,39]. The peak at (1 0 0) decreased for SBA15–NH–PMIDA, which is a sign of a reduction in the mesoscopic order of the structure [39,40]. This may be due to the pore reduction caused by grafted phosphonic groups. The XRD pattern of spent SBA15–NH–PMIDA remained similar to that of the fresh adsorbent. This suggests that the hexagonal structure remained unchanged during adsorption, which is beneficial for repetitive adsorption/desorption.

The BET surface area and BJH pore size distribution analyses of SBA15, SBA15–NH_2 and SBA15–NH–PMIDA were carried out to determine physical properties. According to Table S1, pristine SBA15 recorded a BET surface area of 828 m^2/g, which reduced to 116 m^2/g after modification. This can be due to pore blocking as a result of amine and PMIDA functional groups grafted onto the surface of SBA15. Similar findings were reported by Ryu et al. [39], where BET surface area reduced from 830 m^2/g to 310 m^2/g after amine grafting.

Scanning electron microscopy (SEM) analyses were conducted on powdered SBA15–NH–PMIDA and granular SBA15–NH–PMIDA to observe the surface morphology. The SEM images (Figure 1a) exhibit the well-ordered, 2D, hexagon-structured array of the mesoporous material. Figure 1b shows the image of the surface of the granule, which confirms the synthesis of spherical adsorbents for column studies. Results indicate that the

modified adsorbents were able to maintain a well-ordered structure as that of the virgin SBA15, as previously reported by Ryu et al. [39,40]. The scanning electron microscopy (SEM) images show that our prepared SBA15–NH–PMIDA granular materials are in the micrometer range. Smaller particles generally provide a larger surface area per unit mass, which can enhance the adsorption capacity and diffusion by providing more active sites for pollutant interaction. However, larger particles are typically easier to handle and separate from aqueous solutions after the adsorption process, which can be beneficial for practical applications.

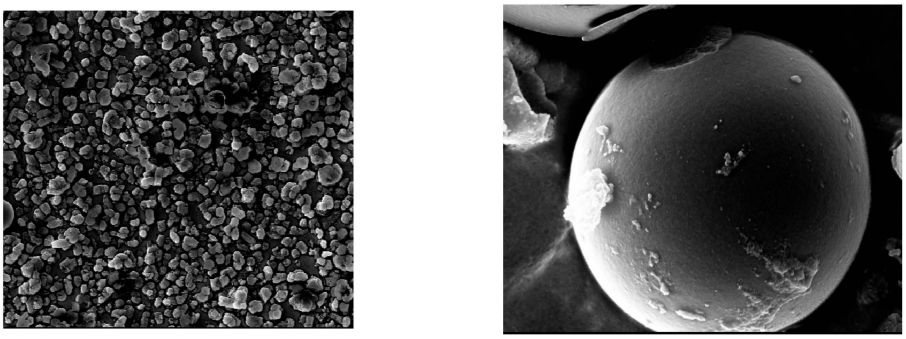

(**a**) (**b**)

Figure 1. SEM images of (**a**) SBA15–NH–PMIDA powder and (**b**) SBA15–NH–PMIDA granule.

3.2. Adsorption Equilibrium

Equilibrium adsorption experiments were conducted with granular SBA15–NH–PMIDA. Beakers containing 50 mL Eu solutions and 0.012 g of SBA15–NH–PMIDA granules at optimum pH 4.75 (refer to Figure S2) were placed in a flat shaker at room temperature (24 °C) for 24 h for equilibrium to be reached. Concentrations of Eu found in AMD are typically quite low so the initial concentrations used were in the range 2.5–30 mg/L. The Langmuir model parameters are shown in Table 4. The adsorption capacity of granular SBA15–NH–PMIDA across different batches was highly consistent, with a 2% error margin.

Table 4. Langmuir Adsorption isotherm parameters for granulated SBA15–NH–PMIDA.

	Q_m (mg/g)	b (L/mg)	R^2
Granulated	57.47	0.97	0.99

3.3. Adsorption Kinetic

Kinetic assessments for granular SBA15 PMIDA were conducted for Eu(III) adsorption at pH 4.75. Initial concentrations were 10 mg/L and 20 mg/L. These were selected for experimental practicality, as extremely low or high concentrations may prove challenging. Equilibrium was achieved within 2 h, where results show a plateau had been established. The kinetic data were analyzed by the surface diffusion model and the results are shown in Table 5.

Table 5. Adsorption kinetic parameters of granular SBA15–NH–PMIDA.

Adsorbent	Initial Con. Eu	Surface Diffusion Model		
		Ks (m/s)	Ds (m^2/s)	R^2
Granular SBA15–NH–PMIDA	10 mg/L 20 mg/L	5.50×10^{-5}	4.00×10^{-17}	0.99 0.99

3.4. Column Experiment for Eu Adsorption Using Granulated SBA15–NH–PMIDA

Column adsorption experiments were executed to investigate the adsorption behavior under diverse operational conditions. These experiments facilitated the examination of design parameters, including filtration velocity, adsorbent medium depth, and influent Eu concentrations, to observe breakthrough trends in adsorption. An initial screening column experiment was initiated with the following conditions: influent Eu concentration = 1 mg/L, flow rate = 1.39×10^{-8} m^3/s, and bed height = 0.1 m. The column experiments were conducted with single solute Eu solutions, as the selectivity of adsorption of Eu in real mining wastewater was high (>80%). The experiment extended over 20 h, during which samples were periodically collected from the outlet and subsequently analyzed for Eu concentration using ICP MS. The column experiments were conducted with short adsorption medium depths (10 and 12.5 cm) in order to obtain the breakthrough in a short time. The experiments were duplicated and the differences in concentration values were less than 2%. A summary of the collected data is presented in Table S2. LDFAM was employed to characterize the behavior of Eu breakthrough curves. The model, developed through Equations (6)–(8) (Table 3) was solved using the PDEPE function in MATLAB, with the coefficients obtained from the analysis presented in Table 3.

3.4.1. Mathematical Modeling of Dynamic Column Behavior

The coefficients derived from the initial column experiment were utilized for modeling the concentration breakthrough at diverse operational conditions and scenarios. This study employed the LDFAM to simulate a variety of breakthrough curves, taking into account factors such as the initial Eu feed concentration, flow rate, and adsorption medium depth. These theoretically obtained curves were then assessed against the corresponding experimental results to gauge the performance of the LDFAM. Figure 2 depicts the validation simulation curve obtained under the initial experimental conditions. All experiments were duplicated to assess the reproducibility of the results. As shown in Figure 1, the experimental results exhibited a notable alignment with the LDFAM. The values of the constants k_f, D_s, and D_L, (Table 6) obtained from this calibration experiment were applied for simulating diverse operating conditions.

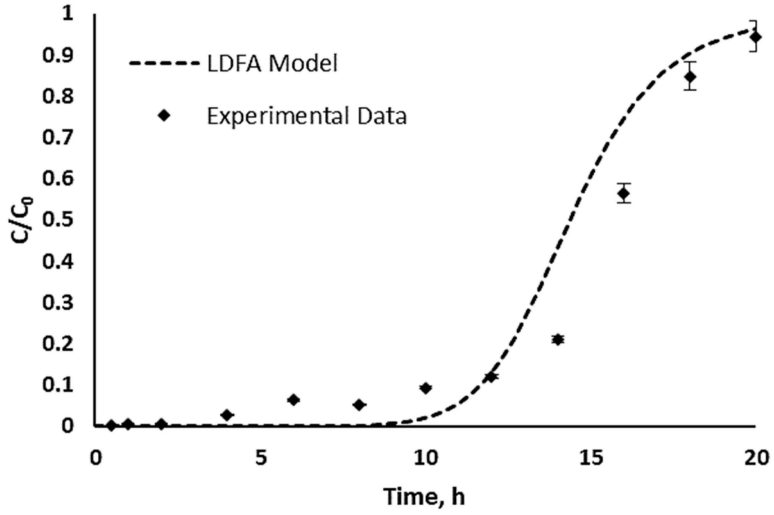

Figure 2. Validation of single solute Eu breakthrough curve for granular SBA15–NH–PMIDA with LDFAM. (Bed height = 0.1 m, linear flow rate = 0.637 m/h, R^2 = 0.95).

Table 6. Parameters obtained from LDFAM (influent Eu concentration = 1 mg/L, flow rate = 1.39×10^{-8} m^3/s, bed height = 0.1 m).

Parameters	Unit	Value
Bed height	m	0.10
Bed diameter	m	0.01
Bed surface area	m^2	7.85×10^{-5}
Flow rate	m^3/s	1.39×10^{-8}
Linear velocity	m/s	1.77×10^{-4}
k_f	m/s	5.50×10^{-5}
D_s	m^2/s	4.00×10^{-17}
D_L (axial dispersion coefficient)	m^2/s	3.00×10^{-6}
C_0	mg/L	1.04

3.4.2. Effect of Initial Concentration

In Figure 3, the experimentally observed results and corresponding theoretical graphs are given for an initial Eu concentration of 3 mg/L, chosen based on the Eu availability in AMD (refer to Table 1). The remaining parameters were kept constant to assess the impact of the concentration on the breakthrough curve (velocity = 0.637 m/h or 1.77×10^{-4} m/s, and bed height = 0.1 m). The same values of the constants k_f, D_s, and D_L (Table 6) were applied to simulate the breakthrough curve (Figure 3). The model exhibited high accuracy (R^2 = 0.92) between model simulation and experimental data, confirming its reliability. With an increase in the initial Eu concentration, the breakthrough curves displayed a more pronounced profile, shifting to the left. Consequently, breakthrough times decreased from 12 to less than 7 h. The exhaustion time was also affected, dropping to less than 10 h when the influent Eu concentration was doubled.

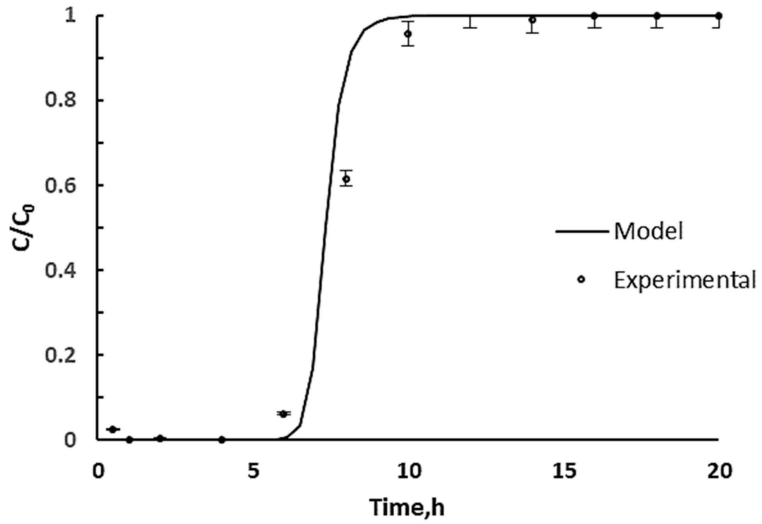

Figure 3. Validation of simulation LDFAM for inlet concentration of 3 mg/L (Bed Height = 0.1 m, velocity = 0.637 m/h, R^2 = 0.92).

3.4.3. Effect of Flowrate

An experiment was conducted with a higher flow rate (0.955 m/h) to examine its impact on the breakthrough curve. The R^2 value of 0.91 indicates a robust fit between the experimental data and the simulation model (see Figure 4). Breakthrough curves simulated at higher flow rates exhibited shorter breakthrough times, and the curves displayed steep profiles, showing faster saturation after the breakthrough period. This phenomenon is attributed to the short residence time at high velocities between the Eu in the solution and the granular SBA15–NH–PMIDA, which is insufficient for reaching equilibrium.

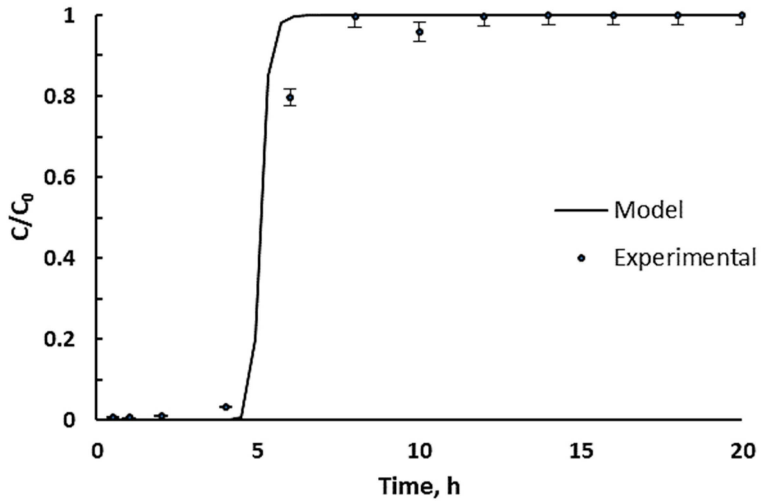

Figure 4. Validation of simulation LDFAM for linear filtration of 0.955 m/h (Inlet concentration = 3 mg/L, bed height = 0.1 m, R^2 = 0.94).

3.4.4. Effect of Adsorbent Medium Depth

The depth of the granular medium is a critical factor. To validate the LDFAM, an experiment was conducted under the following conditions: influent Eu concentration = 3 mg/L; flow rate = 0.637 m/h; bed height = 12.5 cm (see Figure 5). The experimental results closely matched the LDFAM (R^2 = 0.91). As the medium height increased from 10 to 12.5 cm, the breakthrough graphs moved to the right. This indicates that a higher bed height with more adsorbents provided an increased residence time for the Eu ions in the bed.

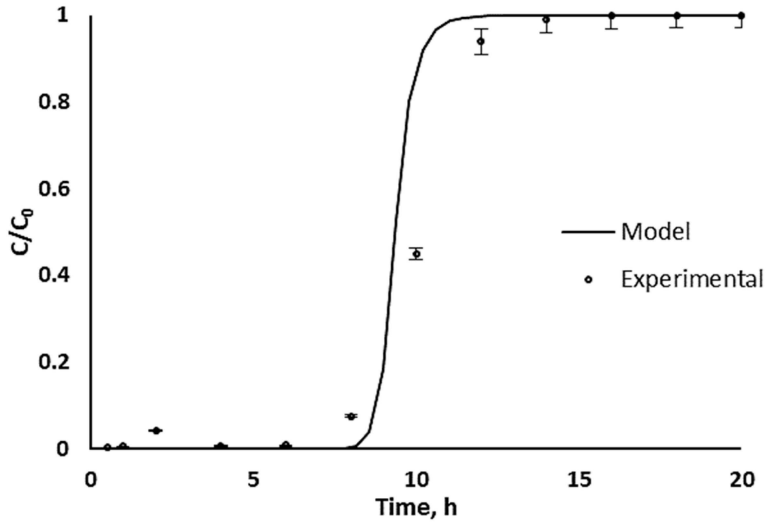

Figure 5. Validation of simulation LDFAM for adsorbent medium depth of 0.125 m (inlet Eu concentration = 3 mg/L, linear filtration rate = 0.637 m/h, R^2 = 0.91).

This study establishes that the LDFAM effectively simulated Eu adsorption on granular SBA15–NH–PMIDA. The model, calibrated with the results of a single representative experiment to determine the axial dispersion coefficient, could then be used with the same coefficient value to simulate dynamic adsorption breakthrough curves under varying operating scenarios, consistently yielding accurate results.

3.5. Adsorbent Reusability Results

The reuse of the adsorbent of SBA15–PMIDA was examined over ten consecutive cycles of adsorption and desorption using real mining wastewater. The chemical composition of mining wastewater in Northern Norway is given in Table 1. Regeneration

was achieved using 0.01 M HCl as the stripping agent for Eu. Following desorption, the adsorbent underwent thorough washing with Milli Q water. Under low pH conditions, the functional ligands protonated, imparting a positive charge to the adsorbent surface. This charge repelled Eu^{3+} ions, facilitating their desorption into the HCl solution.

Table 7 demonstrates that SBA15–PMIDA maintained an adsorption capacity exceeding 85% of its original capacity after ten cycles of adsorption and desorption. This indicates that the regeneration process caused minimal loss of functional groups. Preliminary lab scale results presented in our manuscript are encouraging and suggest that the materials maintain their high adsorption efficiency and structural stability. These results emphasize that the modified SBA15 exhibits superior adsorption capacity and reusability, making it highly suitable for industrial applications. Therefore, pilot-scale experiments should be conducted to evaluate the performance of SBA15–NH–PMIDA under more realistic and large-scale conditions.

Table 7. Recovery of Eu adsorption capacity over 10 cycles of adsorption and desorption (initial concentration = 5 mg of Eu/L; pH = 4.75 ± 0.1).

Cycle	1	2	3	4	5	6	7	8	9	10
Adsorption Capacity (% of original)	100	98	97	96	95	94	93	92	90	87

4. Conclusions

In this investigation, SBA15–NH–PMIDA powder was made into granules by using alginic acid and $CaCl_2$ to facilitate an adsorption study of Eu in a dynamic column set-up. The granulated SBA15–NH–PMIDA showed high adsorptive capacity (57.47 mg/g). The coefficient (D_s) calculated from the kinetic adsorption study utilizing a single-component Eu solution was employed to simulate a break-through curve for the fixed bed column using the LDFAM. The axial dispersion coefficient, calculated through a single column experiment, was subsequently used with the LDFAM to successfully simulate breakthrough curves under various conditions.

The LDFAM exhibited a strong correlation ($R^2 > 0.91$) for diverse operational conditions. The successful application of the LDFAM validates its efficacy as a tool for simulating and optimizing column experiments using granulated SBA15–NH–PMIDA for Eu recovery.

Supplementary Materials: The following supporting information can be downloaded at: https://www.mdpi.com/article/10.3390/su16135636/s1, ref. [58] has been cited in Supplementary Materials.

Author Contributions: Conceptualization, C.F. and S.V.; experiments, C.F.; writing—original draft preparation C.F. and S.R.; review and editing, all the authors; supervision, S.V. and J.K.; project administration, S.V. and H.R. All authors have read and agreed to the published version of the manuscript.

Funding: This project was supported by the University of Technology Sydney grants obtained by S. Vigneswaran. Support by EU ERA-NET Water JPI-2018, Grant 776692: Closing the Water Cycle Gap—Sustainable Management of Water Resources (Water Harmony) and Norwegian Research Council, Grant 322529: Protecting aquatic ecosystem and human health from micropollutants (PATCHER) by Harsha Ratnaweera is also acknowledged.

Institutional Review Board Statement: Not applicable.

Informed Consent Statement: Not applicable.

Data Availability Statement: Data provided in Supplementary Materials.

Conflicts of Interest: The authors declare no conflicts of interest.

References

1. Naidu, G.; Ryu, S.; Thiruvenkatachari, R.; Choi, Y.; Jeong, S.; Vigneswaran, S. A critical review on remediation, reuse, and resource recovery from acid mine drainage. *Environ. Pollut.* **2019**, *247*, 1110–1124. [CrossRef] [PubMed]
2. Ambaye, T.G.; Vaccari, M.; Castro, F.D.; Prasad, S.; Rtimi, S. Emerging technologies for the recovery of rare earth elements (REEs) from the end-of-life electronic wastes: A review on progress, challenges, and perspectives. *Environ. Sci. Pollut. Res.* **2020**, *27*, 36052–36074. [CrossRef]
3. Balaram, V. Rare earth elements: A review of applications, occurrence, exploration, analysis, recycling, and environmental impact. *Geosci. Front.* **2019**, *10*, 1285–1303. [CrossRef]
4. Felipe, E.C.B.; Batista, K.A.; Ladeira, A.C.Q. Recovery of rare earth elements from acid mine drainage by ion exchange. *Environ. Technol.* **2020**, *42*, 2721–2732. [CrossRef] [PubMed]
5. Fonseka, C.; Ryu, S.; Choo, Y.; Naidu, G.; Foseid, L.; Thiruvenkatachari, R.; Kandasamy, J.; Ratnaweera, H.; Vigneswaran, S. Selective Recovery of Europium from real acid mine drainage by using novel SBA15-NH–PMIDA adsorbent and membrane distillation system. *J. Water Proc. Eng.* **2023**, *56*, 104551. [CrossRef]
6. Zhao, F.; Cong, Z.; Sun, H.; Ren, D. The geochemistry of rare earth elements (REE) in acid mine drainage from the Sitai coal mine, Shanxi Province, North China. *Int. J. Coal Geol.* **2007**, *70*, 184–192. [CrossRef]
7. Nordstrom, D.K. Hydrogeochemical processes governing the origin, transport and fate of major and trace elements from mine wastes and mineralized rock to surface waters. *Appl. Geochem.* **2011**, *26*, 1777–1791. [CrossRef]
8. Simate, G.S.; Ndlovu, S. Acid mine drainage: Challenges and opportunities. *J. Environ. Chem. Eng.* **2014**, *2*, 1785–1803. [CrossRef]
9. Rim, K. Effects of rare earth elements on the environment and human health: A literature review. *J. Environ. Health Sci. Eng.* **2016**, *8*, 189–200. [CrossRef]
10. Sahoo, P.K.; Tripathy, S.; Equeenuddin, S.M.; Panigrahi, M.K. Geochemical characteristics of coal mine discharge vis-à-vis behavior of rare earth elements at Jaintia Hills coalfield, northeastern India. *J. Geochem. Explor.* **2012**, *112*, 235–243. [CrossRef]
11. Miekeley, N.; Coutinho de Jesus, H.; Porto da Silveira, C.L.; Linsalata, P.; Morse, R. Rare-earth elements in groundwaters from the Osamu Utsumi mine and Morro do Ferro analogue study sites, Poços de Caldas, Brazil. *J. Geochem. Explor.* **1992**, *45*, 365–387. [CrossRef]
12. Protano, G.; Riccobono, F. High contents of rare earth elements (REEs) in stream waters of a Cu–Pb–Zn mining area. *Environ. Pollut.* **2002**, *117*, 499–514. [CrossRef] [PubMed]
13. Vass, C.R.; Noble, A.; Ziemkiewicz, P.F. The Occurrence and Concentration of Rare Earth Elements in Acid Mine Drainage and Treatment By-products: Part 1—Initial Survey of the Northern Appalachian Coal Basin. *Min. Metall. Explor.* **2019**, *36*, 903–916. [CrossRef]
14. Lecomte, K.L.; Sarmiento, A.M.; Borrego, J.; Nieto, J.M. Rare earth elements mobility processes in an AMD-affected estuary: Huelva Estuary (SW Spain). *Mar. Pollut. Bull.* **2017**, *121*, 282–291. [CrossRef] [PubMed]
15. Olías, M.; Cánovas, C.R.; Basallote, M.D.; Lozano, A. Geochemical behaviour of rare earth elements (REE) along a river reach receiving inputs of acid mine drainage. *Chem. Geol.* **2018**, *493*, 468–477. [CrossRef]
16. Fee, J.A.; Gaudette, H.E.; Lyons, W.B.; Long, D.T. Rare-earth element distribution in Lake Tyrrell groundwaters, Victoria, Australia. *Chem. Geol.* **1992**, *96*, 67–93. [CrossRef]
17. Research, G.V. *Rare Earth Elements Market Size, Share & Trends Analysis Report by Product (Cerium, Dysprosium, Erbium), by Application (Magnets, Catalyst), by Region, and Segment Forecasts, 2019–2025*; Grand View Research: San Francisco, CA, USA, 2019; p. 208.
18. Anastopoulos, I.; Bhatnagar, A.; Lima, E.C. Adsorption of rare earth metals: A review of recent literature. *J. Mol. Liq.* **2016**, *221*, 954–962. [CrossRef]
19. Commission, E. *Report on Critical Raw Materials for the EU: Report of the Ad-hoc Working Group on Defining Critical Raw Materials*; European Commission: Brussels, Belgium, 2014.
20. Commission, E. *Communication from the Commission to the European Parliament, the Council, the European Economic and Social Committee and the Committee of the Regions on the 2017 List of Critical Raw Materials for the EU*; European Commission: Brussels, Belgium, 2017.
21. United States Department of the Interior. *Final List of Critical Minerals*; United States Department of the Interior, Office of the Federal Register, National Archives and Records Administration: Washington, DC, USA, 2018; Volume 83, pp. 23295–23296.
22. Hatch, G.P. Dynamics in the Global Market for Rare Earths. *Elements* **2012**, *8*, 341. [CrossRef]
23. Kumari, A.; Jha, M.K.; Pathak, D.D.; Chakravarty, S.; Lee, J.C. Processes developed for the separation of europium (Eu) from various resources. *Sep. Pur. Rev.* **2019**, *48*, 91–121. [CrossRef]
24. Chen, T.; Yan, B.; Lei, C.; Xiao, X. Pollution control and metal resource recovery for acid mine drainage. *Hydrometallurgy* **2014**, *147–148*, 112–119. [CrossRef]
25. Motsi, T.; Rowson, N.A.; Simmons, M.J.H. Adsorption of heavy metals from acid mine drainage by natural zeolite. *Int. J. Miner. Process.* **2009**, *92*, 42–48. [CrossRef]
26. Sampaio, R.M.M.; Timmers, R.A.; Xu, Y.; Keesman, K.J.; Lens, P.N.L. Selective precipitation of Cu from Zn in a pS controlled continuously stirred tank reactor. *J. Hazard Mater.* **2009**, *165*, 256–265. [CrossRef]
27. Ambiado, K.; Bustos, C.; Schwarz, A.; Bórquez, R. Membrane technology applied to acid mine drainage from copper mining. *Water Sci. Technol.* **2016**, *75*, 705–715. [CrossRef]
28. Das, N.; Das, D. Recovery of rare earth metals through biosorption: An overview. *J. Rare Earths* **2013**, *31*, 933–943. [CrossRef]

29. Hu, Y.; Drouin, E.; Larivière, D.; Kleitz, F.; Fontaine, F.-G. Highly Efficient and Selective Recovery of Rare Earth Elements Using Mesoporous Silica Functionalized by Preorganized Chelating Ligands. *ACS Appl. Mater. Interfaces* **2017**, *9*, 38584–38593. [CrossRef] [PubMed]
30. Xiaoqi, S.; Huimin, L.; Mahurin, S.M.; Rui, L.; Xisen, H.; Sheng, D. Adsorption of rare earth ions using carbonized polydopamine nano carbon shells. *J. Rare Earths* **2016**, *34*, 77–82.
31. Zhang, H.; McDowell, R.G.; Martin, L.R.; Qiang, Y. Selective Extraction of Heavy and Light Lanthanides from Aqueous Solution by Advanced Magnetic Nanosorbents. *ACS Appl. Mater. Interfaces* **2016**, *8*, 9523. [CrossRef]
32. Zheng, X.; Wang, C.; Dai, J.; Shi, W.; Yan, Y. Design of Mesoporous Silica Hybrid Materials as Sorbents for the Selective Recovery of Rare Earth Metals. *J. Mater. Chem. A* **2015**, *3*, 10327. [CrossRef]
33. Lèbre, É.; Corder, G.; Golev, A. The role of the mining industry in a circular economy: A framework for resource management at the mine site level. *J. Ind. Ecol.* **2017**, *21*, 662–672. [CrossRef]
34. Zhao, L.; Duan, X.; Azhar, M.R.; Sun, H.; Fang, X.; Wang, S. Selective adsorption of rare earth ions from aqueous solution on metal-organic framework HKUST-1. *Chem. Engin. J. Adv.* **2020**, *1*, 100009. [CrossRef]
35. Fonseka, C.; Ryu, S.; Choo, Y.; Mullett, M.; Thiruvenkatachari, R.; Naidu, G.; Vigneswaran, S. Selective Recovery of Rare Earth Elements from Mine Ore by Cr-MIL Metal–Organic Frameworks. *ACS Sustain. Chem. Eng.* **2021**, *9*, 16896–16904. [CrossRef]
36. Abdel-Magied, A.F.; Abdelhamid, H.N.; Ashour, R.M.; Zou, X.; Forsberg, K. Hierarchical porous zeolitic imidazolate frameworks nanoparticles for efficient adsorption of rare-earth elements. *Microporous Mesoporous Mater.* **2019**, *278*, 175–184. [CrossRef]
37. Rivas-Sanchez, A.; Cruz-Cruz, A.; Gallareta-Olivares, G.; González-González, R.B.; Parra-Saldívar, R.; Iqbal, H.M. Carbon-based nanocomposite materials with multifunctional attributes for environmental remediation of emerging pollutants. *Chemosphere* **2022**, *303*, 135054. [CrossRef]
38. Chang, F.-Y.; Chao, K.-J.; Cheng, H.-H.; Tan, C.-S. Adsorption of CO_2 onto amine-grafted mesoporous silicas. *Sep. Purif. Technol.* **2009**, *70*, 87–95. [CrossRef]
39. Ryu, S.; Naidu, G.; Moon, H.; Vigneswaran, S. Selective copper extraction by multi-modified mesoporous silica material, SBA-15. *Sci. Total Environ.* **2019**, *697*, 134070. [CrossRef]
40. Ryu, S.C.; Kim, J.Y.; Hwang, M.J.; Moon, H. Recovery of nitrate from water streams using amine-grafted and magnetized SBA-15. *Korean J. Chem. Eng.* **2018**, *35*, 489–497. [CrossRef]
41. Shahbazi, A.; Younesi, H.; Badiei, A. Functionalized SBA-15 mesoporous silica by melamine-based dendrimer amines for adsorptive characteristics of Pb(II), Cu(II) and Cd(II) heavy metal ions in batch and fixed bed column. *Chem. Eng. J.* **2011**, *168*, 505–518. [CrossRef]
42. Da'na, E.; Sayari, A. Adsorption of heavy metals on amine-functionalized SBA-15 prepared by co-condensation: Applications to real water samples. *Desalination* **2012**, *285*, 62–67. [CrossRef]
43. Lee, Y.-R.; Yu, K.; Ravi, S.; Ahn, W.-S. Selective adsorption of rare earth elements over functionalized Cr-MIL-101. *ACS Appl. Mater. Interfaces* **2018**, *10*, 23918–23927. [CrossRef]
44. Ryu, S.; Fonseka, C.; Naidu, G.; Loganathan, P.; Moon, H.; Kandasamy, J.; Vigneswaran, S. Recovery of rare earth elements (Lu, Y) by adsorption using functionalized SBA-15 and MIL-101 (Cr). *Chemosphere* **2021**, *281*, 130869. [CrossRef]
45. Huang, Z.-W.; Li, Z.-J.; Zheng, L.-R.; Wu, W.-S.; Chai, Z.-F.; Shi, W.-Q. Adsorption of Eu(III) and Th(IV) on three-dimensional graphene-based macrostructure studied by spectroscopic investigation. *Environ. Pollut.* **2019**, *248*, 82–89. [CrossRef]
46. Dolatyari, L.; Yaftian, M.R.; Rostamnia, S. Adsorption characteristics of Eu(III) and Th(IV) ions onto modified mesoporous silica SBA-15 materials. *J. Taiwan Inst. Chem. Eng.* **2016**, *60*, 174–184. [CrossRef]
47. Dousti, Z.; Dolatyari, L.; Yaftian, M.R.; Rostamnia, S. Adsorption of Eu (III), Th (IV), and U (VI) by mesoporous solid materials bearing sulfonic acid and sulfamic acid functionalities. *Sep. Sci. Technol.* **2019**, *54*, 2609–2624. [CrossRef]
48. Tan, X.; Fang, M.; Li, J.; Lu, Y.; Wang, X. Adsorption of Eu(III) onto TiO_2: Effect of pH, concentration, ionic strength and soil fulvic acid. *J. Hazard. Mater.* **2009**, *168*, 458–465. [CrossRef] [PubMed]
49. Sun, Y.; Chen, C.; Tan, X.; Shao, D.; Li, J.; Zhao, G.; Yang, S.; Wang, Q.; Wang, X. Retracted Article: Enhanced adsorption of Eu (III) on mesoporous Al_2O_3/expanded graphite composites investigated by macroscopic and microscopic techniques. *Dalton Trans.* **2012**, *41*, 13388–13394. [CrossRef] [PubMed]
50. Suzuki, M. *Adsorption Engineering*; Elsevier Science and Technology: Kodansha, Amsterdam, 1990; pp. 56–62, ISBN I 0444988025.
51. Souza, P.R.; Dotto, G.L.; Salau, N.P.G. Detailed numerical solution of pore volume and surface diffusion model in adsorption systems. *Chem. Eng. Res. Des.* **2017**, *122*, 298–307. [CrossRef]
52. Inglezakis, V.J.; Fyrillas, M.M.; Park, J. Variable diffusivity homogeneous surface diffusion model and analysis of merits and fallacies of simplified adsorption kinetics equations. *J. Hazard. Mater.* **2019**, *367*, 224–245. [CrossRef] [PubMed]
53. Wilke, C.R.; Chang, P. Correlation of diffusion coefficients in dilute solutions. *AICHE J.* **1955**, *1*, 264–270. [CrossRef]
54. García-Mateos, F.J.; Ruiz-Rosas, R.; Marqués, M.D.; Cotoruelo, L.M.; Rodríguez-Mirasol, J.; Cordero, T. Removal of paracetamol on biomass-derived activated carbon: Modeling the fixed bed breakthrough curves using batch adsorption experiments. *Chem. Eng. J.* **2015**, *279*, 18–30. [CrossRef]
55. Lin, X.; Huang, Q.; Qi, G.; Shi, S.; Xiong, L.; Huang, C.; Chen, X. Estimation of fixed-bed column parameters and mathematical modeling of breakthrough behaviors for adsorption of levulinic acid from aqueous solution using SY-01 resin. *Sep. Sci. Technol.* **2017**, *174*, 222–231. [CrossRef]

56. Wakao, N.; Funazkri, T. Effect of fluid dispersion coefficients on particle-to-fluid mass transfer coefficients in packed beds: Correlation of Sherwood numbers. *Chem. Engin. Sci.* **1978**, *33*, 1375–1384. [CrossRef]
57. Gomaa, E.A.; Negm, A.; Tahoon, M.A. Conductometric and volumetric study of copper sulphate in aqueous ethanol solutions at different temperatures. *J. Taibah Univ. Sci.* **2017**, *11*, 741–748. [CrossRef]
58. Fonseka, C. Metals from Mining Wastewater by Membrane/Adsorption Hybrid Systems. Ph.D. Thesis, University of Technology Sydney, Sydney, Australia, 2023.